DOI: https://doi.org/10.2138/am-2018-6522

Revision 1

Vestaite, $(Ti^{4+}Fe^{2+})Ti^{4+}{}_3O_9$, a new mineral in the shocked eucrite Northwest Africa 8003

Run-Lian Pang[1,2], Dennis Harries[2], Kilian Pollok[2], Ai-Cheng Zhang[1,*], and Falko Langenhorst[2,3,*]

[1]State Key Laboratory for Mineral Deposits Research, School of Earth Sciences and Engineering, Nanjing University, Nanjing 210046, China

[2]Institute of Geosciences, Friedrich Schiller University Jena, D-07745 Jena, Germany

[3]Hawai'i Institute of Geophysics and Planetology, School of Ocean and Earth Science and Technology, University of Hawai'i at Manoa, Honolulu, Hawai'i 96822, USA

*Corresponding authors: aczhang@nju.edu.cn; falko.langenhorst@uni-jena.de

For submission to ***American Mineralogist***

ABSTRACT

Our investigations on the shocked eucrite Northwest Africa (NWA) 8003 revealed the occurrence of a new mineral, vestaite [IMA 2017-068; $(Ti^{4+}Fe^{2+})Ti^{4+}_3O_9$]. This mineral coexists with corundum, ilmenite, and Al-Ti-rich pyroxene in shock melt pockets. It has an empirical chemical formula of $(Ti^{4+}_{0.73}Fe^{2+}_{0.63}Al_{0.60}Mn_{0.03}Mg_{0.02}Cr_{0.01})Ti^{4+}_3O_9$ and the monoclinic C2/c structure of schreyerite with a = 17.03(2) Å, b = 4.98(1) Å, c = 7.08(1) Å, β = 106.3(2)°. The ideal vestaite structure can be considered as a modular structure with an alternate intergrowth of M_3O_5-type ($M=Ti^{4+},Fe^{2+},Al$) and Ti_2O_4-type slabs. Alternatively, it can also be envisaged as a crystallographic shear structure with periodically shearing of rutile or α-PbO_2 units. Streaking and splitting of diffraction spots observed in selected area electron diffraction patterns indicate planar defects in the modular structure of vestaite. Our observations reveal that vestaite crystallized at high pressure (≤ 10 GPa) from a melt that represents a mixture of ilmenite and silicate components. A robust constraint on its formation conditions and stability field cannot yet be provided due to the lack of experimental data for these systems. Vestaite is a new, shock-generated mineral first found in a meteorite of the Howardite-Eucrite-Diogenite (HED) clan, the largest achondrite group. Its discovery is not only of significance to the meteoritic mineralogy but could also be of interest to material science.

Keywords: vestaite, new mineral, HED meteorites, shock metamorphism

INTRODUCTION

Meteoritic minerals are important records of the nebular processes in the early solar system and the magmatic processes on the parent bodies of meteorites (e.g., Hazen et al. 2008; Rubin and Ma 2017). From the viewpoint of mineral evolution, secondary processes (such as aqueous alteration and shock metamorphism) on some meteorite parent bodies may result in an increase of the diversity of minerals (Hazen et al. 2008; McCoy 2010; Rubin and Ma 2017; Tomioka and Miyahara 2017). The discovery of each new mineral in meteorites can provide constraints on the dynamic conditions and the history of meteorite parent bodies (Rubin and Ma 2017; Tomioka and Miyahara 2017).

Asteroid 4 Vesta is considered as a protoplanet with a core-mantle-crust structure (Russell et al. 2012) and as the parent body of the Howardite-Eucrite-Diogenite (HED) clan of meteorites, which provide rich information on both the early planetary differentiation and secondary processes of Vesta (e.g., Takeda and Graham 1991; Mittlefehldt 2015). The rock-forming minerals in HED meteorites are pyroxene (orthopyroxene, pigeonite, augite, diopside, hedenbergite) and anorthite. Olivine is less common in most HED meteorites. Accessory minerals include ilmenite, chromite/ulvöspinel, troilite, tridymite, quartz, merrillite, apatite, zircon, baddeleyite, and FeNi metal (Mittlefehldt 2015). Recently, investigations on shock metamorphism of eucrites have revealed the presence of some high-pressure minerals, such as coesite, stishovite, tissintite, vacancy-rich clinopyroxene, super-silicic garnet, and potential grossular, zagamiite (Miyahara et al. 2014; Pang et al. 2016; Fudge et al. 2017, 2018). However, no new minerals have been reported in HED meteorites.

Northwest Africa (NWA) 8003 is a basaltic eucrite that contains both shock melt veins and shock melt pockets. Pang et al. (2016) have identified five high-pressure minerals in this meteorite. During further investigation of NWA 8003, we found a new mineral with the simplified formula $(Ti^{4+}Fe^{2+})Ti^{4+}{}_3O_9$ and a monoclinic *C2/c* structure, which we named "vestaite", after asteroid 4 Vesta. The mineral vestaite has been approved by the Commission on New Minerals, Nomenclature and Classification of the International Mineralogical Association (IMA 2017-068) (Pang et al. 2017). Here we describe the occurrence, chemical composition, crystal structure, and crystal chemistry of this new mineral, and discuss potential implications for the shock metamorphism of NWA 8003.

SAMPLE AND TYPE MATERIALS

NWA 8003 is a basaltic eucrite that was found in 2013 (Ruzicka et al. 2015); our specimen was purchased from a Moroccan dealer in May 2014. It consists mainly of pyroxene and plagioclase, showing a subophitic texture. The accessory minerals are silica polymorphs, ilmenite, troilite, chromite, apatite, merrillite, and zircon. Shock melt veins and pockets are prominently present in NWA 8003. Within or adjacent to the shock melt veins, a few high-pressure minerals have been observed, i.e., coesite, stishovite, tissintite, vacancy-rich clinopyroxene, and super-silicic garnet (Pang et al. 2016).

The type materials of vestaite were discovered in two transmission electron microscope (TEM) foils and are deposited in the Mineralogical Collection of the Friedrich Schiller University Jena, Germany, under the catalog numbers 42073 and 42074, respectively.

ANALYTICAL METHODS

The mineralogical composition and texture of titanium-rich shock melt pockets (hereafter simply melt pockets) was investigated by field emission scanning electron microscopy (Zeiss Supra 55 at Nanjing University, Nanjing, China and FEI Quanta 3D at Institute of Geosciences, Friedrich Schiller University Jena, Jena, Germany). Backscattered electron (BSE) images were taken with both instruments at an accelerating voltage of 15 kV.

Two TEM foils were prepared using focused ion beam (FIB) preparation (ZEISS AURIGA Compact installed at the Institute of Geology and Geophysics, Chinese Academy of Sciences, Beijing; FEI Quanta 3D FEG workstation installed at the Institute of Geosciences, Jena, respectively). Cutting and thinning of these two foils were conducted at an accelerating voltage of 30 kV and various ion beam currents of 30 nA to 0.1 nA. The microtextural and mineralogical characterizations of these two foils were performed by using two FEI Tecnai G^2 F20 TEMs (at Nanjing University and Friedrich Schiller University Jena, respectively), which operate at 200 kV and is equipped with energy-dispersive X-ray (EDX) and electron energy loss spectrometers (EELS). Selected area electron diffraction (SAED), conventional bright-field (BF) imaging, high-resolution (HR) imaging, and scanning transmission electron microscopy (STEM) mode were used to observe the occurrence of vestaite and associated minerals, and to determine the chemical composition and structural data of vestaite.

EDX spectra were recorded using an Oxford X-Max^N 80T SDD system and were quantified by taking an X-ray absorption correction into account (van Cappellen and Doukhan 1994; Langenhorst et al. 1995). Fe and Ti $L_{3,2}$ electron energy loss near-edge structure (ELNES) spectra were measured on vestaite and ilmenite using a Gatan GIF

Quantum. The measurements were performed with an entrance aperture of 2.5 mm and an energy dispersion of 0.05 eV/channel. The energy resolution, visible as the full width at half-maximum height of the zero-loss peak, was 0.85 eV. For the quantification of $Fe^{3+}/\sum Fe$ values we adopted the universal technique by van Aken et al. (1998) and van Aken and Liebscher (2002).

RESULTS

Occurrence of vestaite in NWA 8003

Vestaite in NWA 8003 was identified in two titanium-rich melt pockets (20−30 μm in size), which are enclosed by former plagioclase (now maskelynite, plagioclase, and tissintite), augite, and ilmenite (Figs. 1 and 2). Vestaite occurs as euhedral to subhedral crystals, ~0.2−0.5 μm in width and up to ~2.5 μm in length with normally columnar to platy habit. It is usually associated with corundum, displaying also euhedral to subhedral crystals with 1−2 μm grain sizes. Both vestaite and corundum appear as phenocrysts in a very fine-grained matrix with eutectic to symplectitic textures. The phases in the matrix are Al-Ti-rich pyroxene, secondary Al-bearing ilmenite plus minor troilite (Figs. 2 and 3). No amorphous phases were observed within titanium-rich melt pockets as detected by SAED patterns.

Chemical composition of vestaite

Since vestaite contains considerable amounts of Fe and Ti, the quantification of its composition requires the knowledge of the valence states of these elements. We therefore measured the $L_{3,2}$ electron energy-loss near-edge structures (ELNES) of both elements. The Fe $L_{3,2}$ ELNES spectra show that iron in vestaite is exclusively ferrous (Fig. 4). The quantitative determination of $Fe^{3+}/\sum Fe$ ratio in vestaite is 0.06 ±0.05 by the method in

van Aken et al. (1998) and van Aken and Liebscher (2002) using the universal curve. The ELNES spectra are practically identical to the Fe $L_{3,2}$-edge of ilmenite ($Fe^{3+}/\sum Fe = 0.02 \pm 0.05$) measured in the same FIB section under the same conditions.

The Ti $L_{3,2}$ ELNES spectra of vestaite and ilmenite show a very similar fine structure (Fig. 5) and both are compatible with spectra of Ti^{4+} oxides (Stoyanov et al. 2008), indicating that titanium in vestaite is basically Ti^{4+} in octahedral coordination. We cannot fully rule out the existence of a minor amount of Ti^{3+} (< 5%), because the Ti $L_{3,2}$ edge is relatively insensitive to low Ti^{3+} contents (Stoyanov et al. 2008), but the possible presence of little Fe^{3+} in vestaite is an argument against any Ti^{3+}.

Based on ELNES measurements TEM-EDX analyses were quantified by assuming Fe^{2+} and Ti^{4+}. Averaged TEM-EDX analyses (5 crystals, based on 9 oxygen atoms) of vestaite result in the mean chemical formula $(Ti^{4+}_{0.73}Fe^{2+}_{0.63}Al_{0.60}Mn_{0.03}Mg_{0.02}Cr_{0.01})Ti^{4+}_{3}O_9$. All analyses are listed in Table 1. The sum of the cations ranges from 4.94−5.09 (5.01 on average).

Structural data of vestaite

Single-crystal X-ray studies could not be carried out on vestaite because of its small grain size. The lattice parameters were thus determined from the SAED patterns of various vestaite crystals (Fig. 6). The SAED patterns along ten different zone axes of four different crystals (vst #1, vst #2 and vst #3 from FIB-01; vst #4 from FIB-02) could only be successfully indexed when assuming vestaite possesses the monoclinic *C2/c* crystal structure of schreyerite. No other Ti-bearing oxide structures (e.g., hexagonal $Fe^{3+}_{2}Ti^{4+}_{3}O_9$, Teufer and Temple 1966; Grey and Reid 1975) were compatible with the SAED patterns. The d-spacings of all reflections and their Miller indices are summarized

in Table 2. Based on these data lattice parameters of vestaite were refined using the Unit Cell program (Holland and Redfern 1997). The refined cell parameter are as follows: a=17.03(2) Å, b=4.98(1) Å, c=7.08(1) Å, β=106.3(2)°. The structural model of vestaite illustrated in Fig. 7 is based on the atomic positions of schreyerite (supplementary Table 1), which can be described by alternating structural blocks of M_3O_5 (berdesinskiite structure; V_2TiO_5) and α-PbO_2 (high-pressure structure of TiO_2).

Streaking and splitting of diffraction spots were observed on two of the vestaite crystals (vst # 2 and vst # 4) in this study along [0vw] zone axes (Figs. 6 and 8). These satellite spots indicate a modulated structure and some of the reflections show a lateral displacement from their ideal positions (Fig. 8). In analogy to Harries et al. (2011), three parameters are employed to describe the modulated structure of vestaite: the splitting vector **q‘** (describing the orientation and spacing of modulation interfaces), the fractional shift Δ (describing the displacement of the satellite spots relative to the original spot), and the displacement vector **R** (relating the basic structure and the modulated structure). The geometry of the satellite spots shows that the splitting vector **q‘** is generally oriented along the ***a**** direction but not strictly as indicated by lateral displacements (Fig. 8). The presence of lateral displacements indicates that a two- or three-dimensional interface modulation of the cation occupancy exists in the structure of vestaite. In such case, blocks of perfectly ordered cation arrangements are separated by translational interfaces, across which the neighboring blocks are displaced over a distance |**R**| (Harries et al. 2011).

Geometric relations between the satellite reflections and the main reflections indicate fractional shifts of $\Delta \approx ½$ and $\Delta \approx 0$, respectively (Fig. 8). Based on the known reflection vector **g** of the non-split diffraction spots of the perfect structure, the displace-

ment vector **R** can be determined by the relation $\Delta = \mathbf{g}\cdot\mathbf{R}$ (Van Landuyt et al. 1970). In our study, the displacement vector inferred from the SAED patterns is **R = [¼vw]** with v close to 0 or ½ based on the geometry of the satellite reflections (Fig. 8). This means that the formation of the modulated structure requires the translation operation of the cation sublattice over approximately ¼|**a**| along the **a** direction. However, the displacement vector components v and w cannot be determined since the proper orientation to acquire SAED patterns of vestaite (vst #4) is difficult to achieve. In addition, if the displacement components **v** and **w** are small, it will be difficult to observe the small displacements in the streaky SAED patterns. The inverse length of **q'** indicates that the average spacing of translation interfaces in vestaite is $|1/\mathbf{q'}| \approx 42$ Å in projection along the [010] zone axis (Fig. 8).

DISCUSSION

Chemical variations and substitution mechanisms

Vestaite $(Ti^{4+}Fe^{2+})Ti_3O_9$ is a new member of the Andersson phases that have a general formula $M^{3+}{}_2M^{4+}{}_{n-2}O_{2n-1}$ and monoclinic *C2/c* structure for n=5 (Andersson et al. 1959; Grey and Reid 1972; Grey et al. 1973). The isostructural phases of vestaite include schreyerite $V^{3+}{}_2Ti^{4+}{}_3O_9$, olkhonskite $(Cr^{3+},V^{3+})_2Ti_3O_9$, and machiite $Al^{3+}{}_2Ti^{4+}{}_3O_9$ (Medenbach and Schmetzer 1978; Koneva et al. 1996; Koneva 2002; Döbelin et al., 2006; Krot et al. 2016). The type vestaite in NWA 8003 forms a solid solution between the ideal vestaite (64 mol%) and machiite $Al_2Ti_3O_9$ (30 mol%) with minor other components (6 mol%). This indicates a coupled substitution $Ti^{4+} + Fe^{2+} \Leftrightarrow 2Al^{3+}$ between ideal vestaite and machiite. The ideal vestaite component $(Ti^{4+}Fe^{2+})Ti_3O_9$ is the dominant endmember

(more than 50 mol%) over the machiite component and therefore justifying the guidelines for new minerals (Nickel and Grice 1998).

Our TEM-EDX data show some compositional variations of vestaite (Table 1), which is illustrated in the ternary diagram of $FeTiO_3$-TiO_2-Al_2TiO_5 (Fig. 9). Measured compositions of homogenous crystals (vst #1, vst #2, and vst #5) plot on the binary join vestaite $(Ti^{4+}Fe^{2+})Ti_3O_9$ – machiite $Al^{3+}{}_2Ti_3O_9$ indicating a coupled substitution $Ti^{4+} + Fe^{2+} \rightarrow 2Al^{3+}$ with a general stoichiometry of $A_2B_3O_9$. Small deviations from this binary composition are mainly due to intracrystalline compositional variations, which have been measured in vst #4 and are associated with streaking in its diffraction patterns. In fact, vst #4 has an intracrystalline compositional variation (4.94−5.09 Σcations based on 9 oxygen atoms) larger than the intercrystalline variation between the other four grains (4.98−5.04). In the ternary diagram, the compositions are distributed away from the vestaite-machiite binary along a line, which lies parallel to the TiO_2-$FeTiO_3$ join (Fig. 9). This substitutional character can be best visualized by only focusing on substitutions along a hypothetical $(Ti^{4+}{}_{1.5}\square)Ti_3O_9$-$M^{2+}{}_3Ti_3O_9$ binary (in analogy to TiO_2-$FeTiO_3$ but based on 9 oxygen per formula unit, □ denotes vacancy) in which vestaite $(Ti^{4+}M^{2+})_2Ti_3O_9$ occurs at a $M^{2+}/(M^{2+}+Ti^{4+}-3)$ ratio of 0.5 (Fig. 10). This approach assumes that the B position in vestaite is always completely filled by three Ti^{4+} and that trivalent cations on the A position are not relevant for a deviation from the overall cation sum of 5. Figure 10 indicates a clear correlation of the $M^{2+}/(M^{2+}+Ti^{4+})$ on the A position with the deviation from the ideal stoichiometry. Negative deviations from 5 cations are thus related to the substitution $2Fe^{2+} \rightarrow Ti^{4+} + \square_{cation}$, which can be readily realized by the conversion of a A_2TiO_5 berdesinskiite structural slabs into Ti_2O_4 slabs with α-PbO_2 structure. Positive deviations

from the ideal cation number are related to two possible substitution mechanisms, i.e., $Ti^{4+} + O^{2-} \rightarrow M^{2+} + \square_{oxygen}$, which produces oxygen vacancies that result in $M_2Ti_3O_8\square$ or $Ti^{4+} \rightarrow 2\ M^{2+}$ that can be realized by incorporation of extra M_2TiO_5 slabs in the stacking sequence. Both substitution mechanisms have slightly different slopes in the diagram, but cannot be distinguished by the available data (Fig. 10).

Two structural models of vestaite and its isostructural phases

The Andersson phases $M^{3+}{}_2M^{4+}{}_{n-2}O_{2n-1}$ (n=5) including vestaite share the structure equivalent to synthetic $(Fe^{3+},Cr^{3+})_2Ti^{4+}{}_3O_9$, one of the compounds in the system Cr_2O_3-Fe_2O_3-TiO_2-ZrO_2 with general formula of $(Cr, Fe)_{2p}(Ti,Zr)_{p+2q}O_{5p+4q}$, where p and q are integers (Grey and Reid 1972; Grey et al. 1973). The structure of compounds of this four-component system can be explained by either an ordered intergrowth model or by a crystallographic shear model (Grey and Reid 1972; Grey et al. 1973). In the first model, the structure can be visualized as the ordered intergrowth of p M_3O_5-slab and q M_2O_4-slab. $(Fe^{3+},Cr^{3+})_2Ti^{4+}{}_3O_9$ is the member with p:q=1:1 and its structure is regarded as alternate intergrowth of M_3O_5-type and Ti_2O_4-type slabs. In the case of vestaite, the basic structural units are slabs of $(Ti^{4+},Fe^{2+},Al^{3+})_2TiO_5$ and Ti_2O_4 (Fig. 7).

In the crystallographic shear model, two approaches can be envisaged to generate the structure of $A_2B_3O_9$. The first one is the application of successive crystallographic shear operations on the rutile plane $(132)_r$, determined by equation $(hkl)_{rt}= p(121)_{rt} + q(011)_{rt} = (132)_{rt}$ (rt denotes rutile). Repeated application of shear on rutile plane $(011)_{rt}$ will generate the structural unit of α-PbO_2, while repeated shearing on rutile plane $(121)_{rt}$ will produce the M_3O_5 structural unit. Therefore, successively applying these two types of shear operations on rutile planes will ultimately lead to the alternate intergrowth of

slabs of M_3O_5-type and α-PbO_2-type along the crystallographic shear plane $(132)_{rt}$, generating the $A_2B_3O_9$ structure. Alternately, it is simpler to view the structure of $A_2B_3O_9$ as a sheared α-PbO_2-structure. When applying a shear vector $\frac{1}{2}[010]_{\alpha\text{-}PbO2}$ to the α-PbO_2 structure, the structural unit M_3O_5 will form. Therefore, the structure of $A_2B_3O_9$ can be regarded as the result of periodically applying this shear operation on the α-PbO_2 planes. The crystallographic shear model is a convenient way to illustrate the relationship between $A_2B_3O_9$ and its structural units; however, it does not indicate that the actual formation of $A_2B_3O_9$ proceeds in that way.

The concept of crystallographic shear has been successfully applied in solid state chemistry, such as in case of the non-stoichiometric oxides WO_{3-x}, MO_{3-x}, TiO_{2-x}, Ti_nO_{2n-1}, Mo_nO_{3n-1} and the mixed oxides (e.g., Andersson et al. 1959; Andersson and Wadsley 1966; Bursill and Hyde 1971; Grey and Reid 1972; Grey et al. 1973; Van Landuyt 1974; Langenhorst et al. 2013). However, minerals with crystallographic shear structures are not common in nature (Putnis 1992). Natural occurrences of simple oxides with a crystallographic shear structure such as Ti_3O_5, Ti_4O_7, Ti_5O_9, Ti_6O_{11}, and Ti_8O_{15} have been documented in several interplanetary dust particles and in matrix and Ca-Al-rich inclusion in carbonaceous chondrites (e.g., Rietmeijer and Mackinnon 1990; Brearley 1993; Zhang et al. 2015). As a complex oxide with a crystallographic shear structure, vestaite is the fourth natural occurrence of Andersson phases ($M_2M_{n-2}O_{2n-1}$, n=5) after findings of schreyerite, olkhonskite, and machiite.

Nature of structural defects and their relation to the non-stoichiometry of vestaite

The streaking and splitting of diffraction spots in some of the SAED patterns evidently demonstrate the existence of planar defects. They are usually the result of addi-

tional ordering phenomena superimposing the parental structure, such as defect clustering, vacancy ordering, and cation ordering (e.g., Van Landuyt et al. 1970; Van Dyck 1987; Amelinckx and Van Dyck 1993). Those reflection pairs (small solid circles) situating around the main Bragg reflections (large solid circles) and those appearing around the absent reflections (open circles) define a modulated structure (Fig. 8).

Displacement vector **R** is the key to understand the relation between the superlattice and the parental lattice in the modulated structure. However, the exact **R** could not be determined experimentally in this study as stated before. Only the displacement vector as seen along the [0vw] directions could be estimated based on our SAED patterns, i.e., **R** = [**¼vw**] with v close to 0 or ½. The ideal structural model of $A_2B_3O_9$ provides a clue to the possible displacement vectors across the translation interfaces (Figs. 11a–c). Based on the ideal atom arrangements of vestaite, two possible displacement vectors can be identified, i.e., $\mathbf{R_P} = \frac{1}{16}[48\bar{1}]$ and $\mathbf{R_Q} = \frac{1}{16}[401]$ (Figs. 11d and e). $\mathbf{R_P} = \frac{1}{16}[48\bar{1}]$ applied to a P slab will result in double P slabs in the structure. Similarly, $\mathbf{R_Q} = \frac{1}{16}[401]$ applied to a Q slab will produce double Q slabs in the structure. The small component w = $\pm\frac{1}{16}$ is required to move the displaced cations into the correct configuration with respect to the non-displaced hcp oxygen sublattice and is probably too small to be detected in the streaky SAED patterns, in particular if both displacements occur with similar frequency.

The intercalation of P or Q slabs into an ordered stacking sequence breaks the periodicity of vestaite. The stacking sequence of defective vestaite could be written as -P-Q-P-Q-P-P-Q-P-Q…-P-Q-P-Q-Q-P-Q-P-Q- (viewing down the ***b*** direction). The nature of structural defects in vestaite can either be regarded as the existence of two types of trans-

lation interfaces or antiphase boundaries separating adjacent "domains" of vestaite, or alternatively, as the clustering of "domains" of M_3O_5 and α-PbO_2 in vestaite.

The non-stoichiometry of vestaite is closely related to these defects. Ideal vestaite is an ordered modular compound with alternating P and Q slabs in its structure. Extra P and Q slabs will drive the deviation from the stoichiometry into different directions. An excess of P slabs will result in cation excess, and an excess of Q slabs will result in cation deficit relative to ideal $A_2B_3O_9$. From this perspective of "domains" of M_3O_5 and α-PbO_2, the relatively large chemical variation in the vst #4 can be explained by an inhomogeneous distribution of these two "domain" types (Figs. 10, 11d and e). A good example showing the relation between "microdomains" and non-stoichiometry has been shown in Hazen and Jeanloz (1984) and Putnis (1992). The non-stoichiometry of wüstite $Fe_{1-x}O$ was explained by clusters of "microdomains" of Fe_3O_4 in the structure, indicating that clustering of Fe_3O_4 domains is thermodynamically more favorable than random vacancy distributions when wüstite is quenched (Hazen and Jeanloz 1984; Putnis 1992; Langenhorst et al. 2013). Although the defects in vestaite are more complicated than those in wüstite, the formation mechanism of defect clusters could be similar when a high-temperature origin of vestaite is considered. The formation of these defects could be thermodynamically controlled.

Origin of vestaite

Based on the occurrence and composition of the high-pressure phase (i.e., super-silicic garnet) in shock-induced melt veins, it has been concluded that the crystallization pressure of shock melt veins was in the order of ~10 GPa (Pang et al. 2016). Vestaite in NWA 8003 occurs exclusively in the melt pockets closely adjacent to shock veins (Figs.

1 and 2). Its morphology, chemical composition, coexistence with the high-pressure phase tissintite, and the presence of α-PbO_2 structural blocks point to a crystallization of vestaite at high pressure from a titanium-rich melt. The high Ti contents are a clear indication that ilmenite is an important component in the melt pockets. One of the vestaite-bearing melt pockets appears to be largely enclosed by tissintite and maskelynite and thus the composition of this melt pocket could be approximately a binary ilmenite-plagioclase system. Phase equilibria data are available from melting experiments of ilmenite-anorthite mixtures performed by Lipin and Muan (1974). These experiments were designed to investigate the interrelations among the main titanate phases (ss: solid solution; $ilmenite_{ss}$, $pseudobrookite_{ss}$ and $spinel_{ss}$) in lunar rocks at one atmosphere (Lipin and Muan 1974). A vestaite-like phase is absent in this phase diagram, which strengthens the conclusion of a high-pressure origin of vestaite.

Although the experiments of Lipin and Muan (1974) are not perfectly applicable to the titanium-rich melt pockets, they still provide clues to the minimum temperatures for melt formation. The solidus temperature of the ilmenite-anorthite mixture is around 1200 °C, while the liquidus temperatures ranges between ~1285–1367°C (Lipin and Muan 1974). It is thus reasonable to infer that incipient melting of titanium-rich melt pockets happened at a temperature that was at least higher than the solidus temperature. When taking the pressure effect into account, it is plausible to assume that the temperatures were even higher than the liquidus temperatures determined by Lipin and Muan 1974. However, a better estimation of the formation conditions of vestaite at present is impossible due to lack of high-pressure experiments on analogous or equivalent systems.

IMPLICATIONS

We report here the new mineral vestaite in shock melt pockets from the eucrite NWA 8003. The discovery of vestaite exemplifies that shock metamorphism is the dominating mechanism contributing to the mineral diversification on asteroids like Vesta. In this respect, the finding fits well into the concept of mineral evolution (e.g., Hazen et al., 2008; McCoy 2010; Tomioka and Miyahara 2017;) and demonstrates that shock melt veins and pockets in natural samples are potential sources for new minerals, especially new high-pressure phases. Most newly found minerals in shocked meteorites were formed by crystallization from high-pressure monomineralic melts or via solid transformation from a primary phase, such as tissintite, liebermannite, zagamiite, and riesite (Langenhorst and Poirier 2000a, 2000b; Ma et al. 2015, 2018; Ma and Tschauner 2017; Tschauner et al. 2017). The discovery of vestaite draws our attention to the melt interactions between two or more paternal minerals under high-pressure and high-temperature shock conditions. Experimental data on high-pressure phase equilibria in the ilmenite-silicate mixing system are required to constrain the formation conditions of vestaite. We suggest that similar mineral assemblages with vestaite can be expected in shocked meteorites with Ti-rich phases. The observation of such phases may provide further insights into the collisional history of shocked meteorites and their parent bodies.

Moreover, the modulated crystal structure and non-stoichiometric composition of vestaite could be of interest to material scientists. Its isostructural phases, which have the general formula $A_2B_3O_9$, consist of cations with different charges (e.g., Fe^{2+}, Mg^{2+}, Mn^{2+}; Al^{3+}, Cr^{3+}, Fe^{3+}, REE^{3+},V^{3+}; V^{4+}, Ti^{4+}, Zr^{4+}), showing the high variability of this structure type. Compounds of mixed metal oxides, such as ABO_3 perovskite, AB_2O_4 spinel, and pseudobrookite, have extensive industrial and technological applications due to their re-

markable physical properties (e.g., Dondi et al. 2007; Wachs and Routray 2012). As a new iron-aluminum-titanium oxide, vestaite or schreyerite-structured compounds could be of potential use in industrial applications.

ACKNOWLEDGMENTS

This work was supported by the National Natural Science Foundation of China (Grant 41673068), the Natural Science Foundation of Jiangsu Province of China (Grant BK20170017), and the Gottfried Wilhelm Leibniz program of the Deutsche Forschungsgemeinschaft (LA830/14-1). Li-Xin Gu, Agnese Fazio, and Jia-Ni Chen are appreciated for their technical assistance during preparing FIB foils, SEM, and TEM observations. The first author is also grateful to the China Scholarship Council for a 2 years PhD grant and to the group of Analytical Mineralogy of Micro- and Nanostructures, Friedrich Schiller University Jena for hosting her during this period. We thank Chi Ma and Erin Walton for their helpful reviews that improved the quality of the paper, and associate editor Steve Simon for his comments and editorial handling.

REFERENCES CITED

Amelinckx, S., and Van Dyck, D. (1993) Electron diffraction effects due to modulated structures. In J.M. Cowley, ED., Electron Diffraction Techniques, 2, 309–373, IUCr/Oxide Science Publications.

Andersson, S., and Wadsley, A.D. (1966) Crystallographic shear and diffusion paths in certain higher oxides of niobium, tungsten, molybdenum and titanium. Nature, 211, 581–583.

Andersson, S., Sundholm, A., and Magnéli, A. (1959) A homologous series of mixed titanium chromium oxides $Ti_{n-2}Cr_2O_{2n-1}$ isomorphous with the series Ti_nO_{2n-1} and V_nO_{2n-1}. Acta Chemica Scandinavica, 13, 989–997.

Armbruster, T., Galuskin, E.V., Reznitsky, L.Z., and Sklyarov, E.V. (2009) X-ray structural investigation of oxyvanite (V_3O_5)-berdesinskiite (V_2TiO_5) series: V^{4+} substituting for octahedrally coordinated Ti^{4+}. European Journal of Mineralogy, 21, 885–891.

Bernhardt, H.J., Schmetzer, K., and Medenbach, O. (1983) Berdesinskiite, V_2TiO_5, a new mineral from Kenya and additional data for schreyerite, $V_2Ti_3O_9$. Neues Jahrbuch für Mineralogie-Monatsshefte, 3, 110–118.

Brearley, A.J. (1993) Occurrence and possible significance of rare Ti oxides (Magnéli phases) in carbonaceous chondrite matrices. Meteoritics, 28, 590–595.

Bursill, L.A., and Hyde, B.G. (1971) Crystal structures in the {1-32} CS family of higher titanium oxides Ti_nO_{2n-1}. Acta Crystallographica, B27, 210–215.

Dondi, M., Matteucci, F., Cruciani, G., Gasparotto, G., and Tobaldi. D.M. (2007) Pseudobrookite ceramic pigments: crystal structural, optical and technological properties. Solid State Sciences, 9, 362–369.

Döbelin, N., Rezinitsky, L.Z., Sklyarov, E.V., Armbruster, T., and Medenbach, O. (2006) Schreyerite, $V_2Ti_3O_9$, new occurrence and crystal structure. American Mineralogist, 91, 196–202.

Fudge, C., Sharp, T.G., Ma, C., Hu, J., Wittmann, A., and Tschauner, O. (2017) Northwest Africa 10658, a uniquely shocked eucrite with a range of deformation, trans-

formation and recrystallization effects. Meteoritics & Planetary Science, 52, S1 (Abstract # 6297).

Fudge, C., Sharp, T.G., Hu, J., Ma, C., Tschauner, O., and Wittmann, A. (2018) Characterization of a new high-pressure assemblage after anorthitic plagioclase in polymict eucrite Northwest Africa 10658. 49th Lunar and Planetary Science Conference (Abstract # 2083).

Grey, I.E., and Reid, A.F. (1972) Shear structure compounds $(Cr,Fe)_2Ti_{n-2}O_{2n-1}$ derived from the α-PbO_2 structural type. Journal of Solid State Chemistry, 4, 186–194.

Grey, I.E., and Reid, A.F. (1975) The structure of pseudorutile and its role in the natural alteration of ilmenite. American Mineralogist, 60, 898–906.

Grey, I.E., Reid, A.F., and Allpress, J.G. (1973) Compounds in the system Cr_2O_3-Fe_2O_3-TiO_2-ZrO_2 based on intergrowth of the α-PbO_2 and V_3O_5 structural types. Journal of Solid State Chemistry, 8, 86–99.

Harries, D., Pollok, K., and Langenhorst, F. (2011) Translation interface modulation in NC-pyrrhotites: Direct imaging by TEM and a model toward understanding partially disordered structural states. American Mineralogist, 96, 716–731.

Hazen, R.M., and Jeanloz, R. (1984) Wüstite ($Fe_{1-x}O$): A review of its defect structure and physical properties. Review of Geophysics and Space Physics, 22, 37–46.

Hazen, R.M., Papineau, D., Bleeker, W., Downs, R.T., Ferry, J.M., McCoy, T.J., Sverjensky, D.A., and Yang, H. (2008) Mineral evolution. American Mineralogist, 93, 1693–1720.

Holland, T.J.B., and Redfern, S.A.T. (1997) Unit cell refinement from powder diffraction data: the use of regression diagnostics. Mineralogical Magazine, 61, 65–77.

Krot, A.N. (2016) Machiite, IMA 2016-067. CNMNC Newsletter No. 34, December 2016, page 1317. Mineralogical Magazine, 80, 1315–1321.

Koneva, A.A. (2002) Cr-V oxides in metamorphic rocks, Lake Baikal, Russia. Neues Jahrbuch für Mineralogie-Monatshefte, 12, 541–550.

Koneva, A.A., Piskunova, L.F., Ushchapovskaya, Z.F., and Konev, A.A. (1996) Olkhonskite $(Cr,V)_2Ti_3O_9$ — A new mineral from the Priolkhon'ye (Abstract). American Mineralogist, 81, 251–252.

Langenhorst, F., and Poirier, J.P. (2000a) "Eclogitic" minerals in a shocked basaltic meteorite. Earth and Planetary Science Letters, 176, 259−265.

Langenhorst, F., and Poirier, J.P. (2000b) Anatomy of black veins in Zagami: clues to the formation of high-pressure phases. Earth and Planetary Science Letters, 184, 37−55.

Langenhorst, F., Joreau, P., and Doukhan, J.C. (1995) Thermal and shock metamorphism of the Tenham chondrite: A TEM examination. Geochimica et Cosmochimica Acta, 59, 1835−1845.

Langenhorst, F., Harries, D., and Pollok, K. (2013) Non-stoichiometry, defects, and superstructures in sulfide and oxide minerals. In F. Nieto and K.J.T. Livi, Eds., Minerals at Nanoscale, 14, 261−294. EMU Notes in Mineralogy, European Mineralogical Union and the Mineralogical Society of Great Britain and Ireland.

Lipin, B.R., and Muan, A. (1974) Equilibria bearing on the behavior of titanate phases during crystallization of iron silicate melts under strongly reducing conditions. Lunar and Planetary Science Conference Proceedings, 5, 535–548.

Ma, C. and Tschauner, O. (2017) Zagamiite, IMA 2015-022a. CNMNC Newsletter No. 36, April 2017, page 409. Mineralogical Magazine, 81, 403–409.

Ma, C., Tschauner, O., Beckett, J.R., Liu, Y., Rossman, G.R., Zhuravlev, K., Prakapenka, V., Dera, P., and Taylor, L.A. (2015) Tissintite, (Ca,Na,□)$AlSi_2O_6$, a highly-defective, shock-induced, high-pressure clinopyroxene in the Tissint martian meteorite. Earth and Planetary Science Letters, 422, 194–205.

Ma, C., Tschauner, O., Beckett, J.R., Rossman, G.R., Prescher, C., Prakapenka, V.B., Bechtel H.A., and Macdowell, A. (2018) Liebermannite, $KAlSi_3O_8$, a new shock-metamophic, high-pressure mineral from the Zagami Martian meteorite. Meteoritics & Planetary Science, 53, 50−61.

McCoy, T.J. (2010) Mineralogical evolution of meteorites. Elements, 6, 19–23.

Medenbach, O., and Schmetzer, K. (1978) Schreyerite, $V_2Ti_3O_9$, a new mineral. American Mineralogist, 63, 1182–1186.

Mittlefehldt, D.W. (2015) Asteroid (4) Vesta: I. The howardite-eucrite-diogenite (HED) clan of meteorites. Chemie der Erde–Geochemistry, 75, 155–183.

Miyahara, M., Ohtani, E., Yamaguchi, A., Ozawa, S., Sakai, T.S., and Hirao, N. (2014) Discovery of coesite and stishovite in eucrite Proceedings of the National Academy of Sciences, 111, 10939–10942.

Momma, K., and Izumi, F. (2011) VESTA 3 for three-dimensional visualization of crystal, volumetric and morphology data. Journal of Applied Crystallography, 44, 1272–1276.

Nickel, E.H., and Grice, J.D. (1998) The IMA Commission on New Minerals and Mineral Names: procedures and guidelines on mineral nomenclature, 1998. Mineralogy and Petrology, 64, 237–263.

Pang, R.L., Zhang, A.C., Wang, S.Z., Wang, R.C., and Yurimoto, H. (2016) High-pressure minerals in eucrite suggest a small source crater on Vesta. Scientific Reports, 6, 26063.

Pang, R.L., Harries, D., Pollok, K., Zhang, A.C., and Langenhorst, F. (2017) Vestaite, IMA 2017-068. CNMNC Newsletter No. 40, December 2017, page 1578. Mineralogical Magazine, 81, 1577–1581.

Putnis, A. (1992) Defects in minerals. In An Introduction to Mineral Sciences, p. 185–237. Cambridge University Press, U.K.

Rietmeijer, F.J.M., and Mackinnon, I.D. (1990) Titanium oxide Magnéli phases in four chondritic porous interplanetary dust particles. Proceedings of the 20th Lunar and Planetary Science Conference, 20, 323–333.

Rubin, A.E., and Ma, C. (2017) Meteoritic minerals and their origins. Chemie der Erde–Geochemistry, 77, 325–385.

Russell, C.T., Raymond, C.A., Coradini, A., McSween, H.Y., Zuber, M.T., Nathues, A., De Sanctis, M.C., Jaumann, R., Konopliv, A.S., Preusker, F., and others. (2012) Dawn at Vesta: Testing the protoplanetary paradigm. Science, 33, 684–686.

Ruzicka, A., Grossman, J., Bouvier, A., Herd, C.D.K. and Agee, C.B. (2015) The Meteoritical Bulletin, No. 102. Meteoritics & Planetary Science, 50, 1662–1662.

Stoyanov, E., Langenhorst, F., and Steinle-Neumann, G. (2008) The effect of valence state and site geometry on Ti $L_{3,2}$ and O K electron energy-loss spectra of Ti_xO_y phases. American Mineralogist, 92, 577–586.

Takeda, H., and Graham, A.L. (1991) Degree of equilibration of eucritic pyroxenes and thermal metamorphism of the earliest planetary crust. Meteoritics, 26, 129–134.

Teufer, G., and Temple, A.K. (1966) Pseudorutile—a new mineral intermediate between ilmenite and rutile in the N alteration of ilmenite. Nature, 211, 179.

Tschauner, O., Ma, C., Lanzirotti, A., and Newville, M. (2017) Riesite, a new high pressure polymorph of TiO_2 that forms upon shock-release-comparison to $(Zr,Ti)O_2$ in pseudotachylites. Goldschmidt 2017 (Abstract).

Tomioka, N., and Miyahara, M. (2017) High-pressure minerals in shocked meteorites. Meteoritics & Planetary Science, 52, 2017−2039.

Van Aken, P.A., and Liebscher, B. (2002) Quantification of ferrous/ferric ratios in minerals: new evaluation schemes of Fe L_{23} electron energy-loss near-edge spectra. Physics and Chemistry of Minerals, 29, 188–200.

Van Aken, P.A., Liebscher, B., and Styrsa, V.J. (1998) Quantitative determination of iron oxidation states in minerals using Fe $L_{2,3}$-edge energy-loss near-edge structure spectroscopy. Physics and Chemistry of Minerals, 25, 323–327.

Van Cappellen, E., and Doukhan, J.C. (1994) Quantitative transmission X-ray microanalysis of ionic compounds. Ultramicroscopy, 53, 343–349.

Van Dyck, D., Broddin, D., Mahy, J., and Amelinckx, S. (1987) Electron diffraction of translation interface modulated structures. Physica Status Solidi (a), 103, 357–373.

Van Landuyt, J. (1974) Shear structure and crystallographic shear propagation. Le Journal de Physique Colloques, 35, C7, 53–63.

Van Landuyt, J., De Ridder, R., Gevers, R., and Amelinckx, S. (1970) Diffraction effects due to shear structures: a new method for determining the shear vector. Material Research Bulletin, 5, 353–362.

Wachs, I.E., and Routray, K. (2012) Catalysis science of bulk mixed oxides. American Chemical Society Catalysis, 6, 1235−1246.

Zhang, A.C., Ma, C., Sakamoto, N., Wang, R.C., Hsu, W.B., and Yurimoto, H. (2015) Mineralogical anatomy and implications of a Ti-Sc-rich ultra-refractory inclusion from Sayh al Uhaymir 290 CH3 chondrite. Geochimica et Cosmochimica Acta, 163, 27–39.

FIGURE CAPTIONS

Figure 1. (a)-(d) Backscattered electron (BSE) images show the distribution of titanium-rich melt pockets. These titanium-rich melt pockets are hosted in the rock fragments, which are entrained into the shock melt veins. Two of them are enlarged and shown in (b) and (d), respectively. The locations of FIB sections (FIB-01 and FIB-02) are marked with the white rectangles in (b) and (d). Ilm: ilmenite; Opx: orthopyroxene; Aug: augite; Pl glass: plagioclase glass; Tiss-I: tissintite-I; Crn: corundum; Vst: vestaite; Ti-rich MP: titanium-rich melt pocket.

Figure 2. BSE image shows the depth profile of one titanium-rich melt pocket (shown in Fig. 1d). The interface between the primary ilmenite and titanium-rich melt pocket can be seen in this profile. Vst: vestaite; Crn: corundum; Ilm: ilmenite; Px: pyroxene; Cal: calcite (secondary).

Figure 3. (a)-(b) HAADF-STEM images show the microtexures of two titanium-rich melt pockets in Fig. 1b and Fig. 1d, respectively. These two titanium-rich melt pockets contain similar mineral assemblages but show different textures. Minerals in these two melt pockets include vestaite, corundum, ilmenite, Al-Ti-rich pyroxene, and troilite. Vst: vestaite; Crn: corundum; Tro: troilite; Ilm: ilmenite; Px: pyroxene.

Figure 4. Fe $L_{3,2}$ ELNES spectra of vestaite (vst #4) and Al-bearing ilmenite in Fig. 3b. Two grey columns represent the integrating windows of 2 eV width from 708.5 eV to 710.5 eV and from 719.7 eV to 721.7 eV used for the determination of $I(L_3)/I(L_2)$. The universal curve of $I(L_3)/I(L_2)$ versus $Fe^{3+}/\sum Fe$ from van Aken et al. (1998) and van Aken

and Liebscher (2002) are applied to quantitatively determine the $Fe^{3+}/\sum Fe$ ratio. The red lines represent the double arctan background subtraction function.

Figure 5. The Ti $L_{3,2}$-edge ELNES spectra of vestaite (vst #4) and Al-bearing ilmenite shown in Fig. 3b. The Ti $L_{3,2}$ ELNES spectra of vestaite and ilmenite in our sample NWA 8003 are fully consistent with Ti^{4+} in octahedral coordination.

Figure 6. (a)-(d) The SAED patterns of vestaite along the [205], [011], [100], and [010] zone axes are taken from different vestaite crystals. Two of the vestaite crystals (vst #2 and vst #4) are shown in Fig. 3a and Fig. 3b, respectively. The other two (vst #1 and vst #3) are from the FIB-01 section but are not shown in the HAADF-STEM image. The streaking and splitting of the diffraction spots along the **a*** direction could be observed in (b) and (d).

Figure 7. (a-c) Idealized structural model of $A_2B_3O_9$, M_3O_5 (berdesinskiite V_2TiO_5, Bernhardt et al. 1983; Armbruster et al. 2006) and α-PbO_2 (high-pressure polymorph of rutile). $A_2B_3O_9$ can be considered as alternate intergrowth of V_2TiO_5-type and α-PbO_2-type slabs. The corner-shared octahedra chains (cation site B, in blue) running along the [001] direction accommodate only Ti^{4+}. The face-sharing octahedral pairs (cation site A, in red) show an arrangement as in corundum and are occupied by Ti^{4+}, Al^{3+}, and M^{2+}. The structural models are generated using the VESTA (Visualization for Electronic and STructural Analysis) package (Momma and Izumi 2011).

Figure 8. (a) Close-up of the SAED diffraction pattern of vestaite (vst #4) in Fig. 6d. (b) Simplified scheme of the splitting spots drawing. The open circles represent the absent reflections. The red dots are the observed spots in the SAED image. The size difference

represents their intensity contrast qualitatively. The lateral shifts of the satellite spots from the **a*** direction are slight but observable (indicated by red arrows), implying the orientation anomalies of structural defects. The parallelogram defined by the four main Bragg reflections represents the reciprocal lattice of idealized vestaite. The d-spacing values of (200) and (002) are 16.2 Å and 6.8 Å, respectively. Note that only the sharp satellite spots are drawn in this scheme for the sake of simplicity. Δ: fractional shift ($0 \leqslant \Delta < 1$); **g**: diffraction vector; **R:** displacement vector; **q'**: splitting vector; **1/q':** inverse length of **q'**, describing the average spacing of defects-related planes.

Figure 9. Ternary diagram of $FeTiO_3$-TiO_2-Al_2TiO_5 illustrates the compositions of vestaite. The white circles represent the composition of vestaite grain (vst #4), which shows large composition variations. The grey circles represent the compositions of other vestaite grains (vst #1, vst #2, vst #3 and vst #5). Note that some of them are overlapping. The star on the $(TiFe)Ti_3O_9$-$Al_2Ti_3O_9$ tieline marks the position of intermediate member, i.e., 50 mol% machiite and 50 mol% end member vestaite $(TiFe)Ti_3O_9$. $Fe_2Ti_3O_8\square$ and $(Ti_{1.5}\square_{0.5})Ti_3O_9$ are the hypothetical members, □ denotes vacancy.

Figure 10. Binary plot of sum cations vs. $M^{2+}/(M^{2+}+Ti^{4+}-3)$ ratio of vestaite in NWA 8003. Note that one of vestaite crystals (vst #4) exhibits large compositional variations. Trend lines a, b and c represent different substitution mechanisms. Trend **a** denotes the substitution $2M^{2+} \rightarrow Ti^{4+} + \square_{cation}$. Trends **b** and **c** represent the substitution relations $Ti^{4+} \rightarrow 2M^{2+}$ and $Ti^{4+} + O^{2-} \rightarrow M^{2+} + \square_{oxygen}$, respectively.

Figure 11. (a)-(c) Idealized structural models of M_3O_5 (labelled P), α-PbO_2 (labelled Q) and $A_2B_3O_9$ (see also Fig. 7a). The unit cell of vestaite is highlighted by the dashed box in (c). (d)-(e) Atomic configurations of vestaite with extra P and Q slab. The displacement

vectors $\mathbf{R_P}$ and $\mathbf{R_Q}$ are obtained assuming that the O atoms remain in a coherent hexagonal close-packing (hcp) configuration across the translation interface. Small open circles represent O atoms, blue spheres represent octahedral Ti atoms and red sphere pairs represent the face-sharing octahedral Al, Ti and Fe (Mg, Mn) atoms. Black dashed lines represent the translation interface.

Table 1. Compositions acquired by TEM-EDX for vestaite in NWA 8003

	Vestaite #1	**Vestaite #2**	**Vestaite #3**	**Vestaite #3**	**Vestaite #4**	**Vestaite #4**	**Vestaite #4**	**Vestaite #4**	**Vestaite #4**	**Vestaite #4**	**Vestaite #5**	**Avg. (#1-#5)[a]**	**S.D.**
TiO_2	79.1	79.7	79.4	78.5	77.0	77.5	76.4	81.2	80.3	77.3	78.8	79.0	0.45
Al_2O_3	7.67	7.99	7.72	7.54	9.57	9.24	9.81	8.40	8.45	9.31	8.22	8.13	0.54
Cr_2O_3	0.17	0.27	0.00	0.14	0.28	0.17	0.25	0.14	0.26	0.20	0.22	0.19	0.07
MgO	0.00	0.00	0.26	0.29	0.33	0.42	0.41	0.28	0.28	0.41	0.37	0.20	0.17
FeO	12.2	12.0	12.6	12.6	12.5	12.7	12.4	10.0	10.7	12.7	11.4	12.0	0.39
MnO	0.94	0.00	0.00	0.93	0.38	0.00	0.75	0.00	0.00	0.00	0.94	0.51	0.38
Total	100.0	100.0	100.0	100.0	100.0	100.0	100.0	100.0	100.0	100.0	100.0	100.0	
						Calculated on the basis of 9 oxygen atoms							
Ti	3.741	3.746	3.739	3.737	3.628	3.653	3.617	3.777	3.751	3.639	3.733	3.727	0.025
Al	0.570	0.589	0.571	0.563	0.707	0.683	0.729	0.613	0.619	0.687	0.611	0.602	0.039
Cr	0.008	0.013	0.000	0.007	0.014	0.008	0.013	0.007	0.013	0.010	0.011	0.009	0.003
Mg	0.000	0.000	0.025	0.028	0.031	0.040	0.039	0.026	0.026	0.039	0.035	0.019	0.016
Fe	0.639	0.629	0.660	0.664	0.652	0.662	0.652	0.515	0.556	0.666	0.600	0.629	0.021
Mn	0.050	0.000	0.000	0.050	0.020	0.000	0.040	0.000	0.000	0.000	0.050	0.027	0.020
O	9.000	9.000	9.000	9.000	9.000	9.000	9.000	9.000	9.000	9.000	9.000	9.000	
ΣCations	5.008	4.977	4.994	5.049	5.053	5.046	5.091	4.938	4.965	5.040	5.040	5.014	0.021

[a]: calculated after averaging the compositions of vst #3 and vst #4, representing the mean composition of five vestaite crystals.
S.D.: standard deviation.

Table 2. The observed and calculated d-spacing values of vestaite

d (observed, Å)	d (calculated, Å)	h	k	l
8.17	8.17	2	0	0
4.76	4.76	1	1	0
4.08	4.09	4	0	0
4.06	4.06	1	1	-1
3.76	3.76	1	1	1
3.66	3.68	3	1	0
3.53	3.52	3	1	-1
3.50	3.50	-2	0	2
3.40	3.40	0	0	2
3.01	3.00	3	1	1
2.86	2.88	1	1	-2
2.78	2.77	-3	1	2
2.77	2.77	5	1	-1
2.66	2.66	1	1	2
2.48	2.49	0	2	0
2.42	2.49	-6	0	2
2.43	2.43	-5	1	2
2.35	2.35	5	-1	1
2.18	2.18	7	1	-1
2.05	2.04	7	1	-2
2.01	2.01	0	2	2
1.94	1.93	-4	2	2
1.89	1.89	7	-1	1
1.76	1.77	9	-1	1
1.58	1.58	2	0	4
1.57	1.57	8	2	-2
1.48	1.49	-3	3	2
1.47	1.47	1	3	2
1.43	1.42	-5	3	2

Supplementary table 1. Factional coordinates of atoms for schreyerite[a] and vestaite

Schreyerite	Atom	Label	x	y	z	Occupancy
1	V	V3	-0.07555	-0.50100	0.10036	0.893
2	Cr	Cr3	-0.07555	-0.50100	0.10036	0.079
3	Fe	Fe3	-0.07555	-0.50100	0.10036	0.018
4	Ti	Ti1	0.00000	0.00000	0.00000	0.845
5	V	V1	0.00000	0.00000	0.00000	0.156
6	Ti	Ti2	-0.21608	0.00670	-0.07227	0.845
7	V	V2	-0.21608	0.00670	-0.07227	0.156
8	O	O1	-0.10850	0.15850	-0.02030	1
9	O	O2	-0.17420	-0.33160	0.07310	1
10	O	O3	-0.04740	-0.34630	-0.13000	1
11	O	O4	-0.22620	-0.16790	-0.31900	1
12	O	O5	0.00000	0.19650	-0.25000	1
Vestaite	**Atom**	**Label**	**x**	**y**	**z**	**Occupancy[b]**
1	Ti	Ti3	-0.07555	-0.50100	0.10036	0.333
2	Fe	Fe1	-0.07555	-0.50100	0.10036	0.333
3	Al	Al1	-0.07555	-0.50100	0.10036	0.333
4	Ti	Ti2	0.00000	0.00000	0.00000	1
5	Ti	Ti1	-0.21608	0.00670	-0.07227	1
6	O	O1	-0.10850	0.15850	-0.02030	1
7	O	O2	-0.17420	-0.33160	0.07310	1
8	O	O3	-0.04740	-0.34630	-0.13000	1
9	O	O4	-0.22620	-0.16790	-0.31900	1
10	O	O5	0.00000	0.19650	-0.25000	1

[a]: The factional coordinates of atoms of schreyerite is taken from Döbelin et al. (2006).
[b]: The actual atomic occupancy of Ti, Fe, Al is not available and assumed equal in structural site A in vestaite.

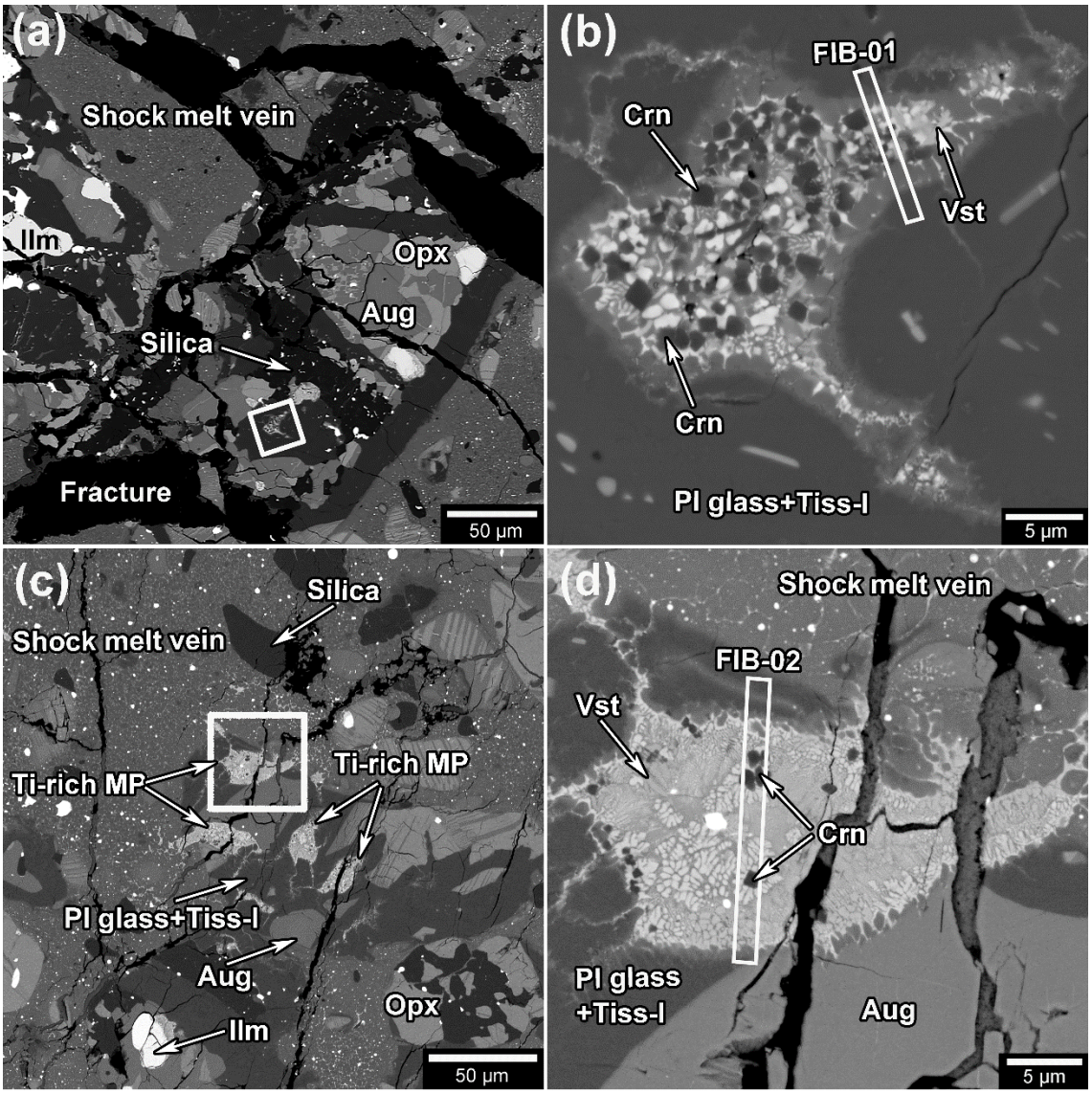

Figure 1

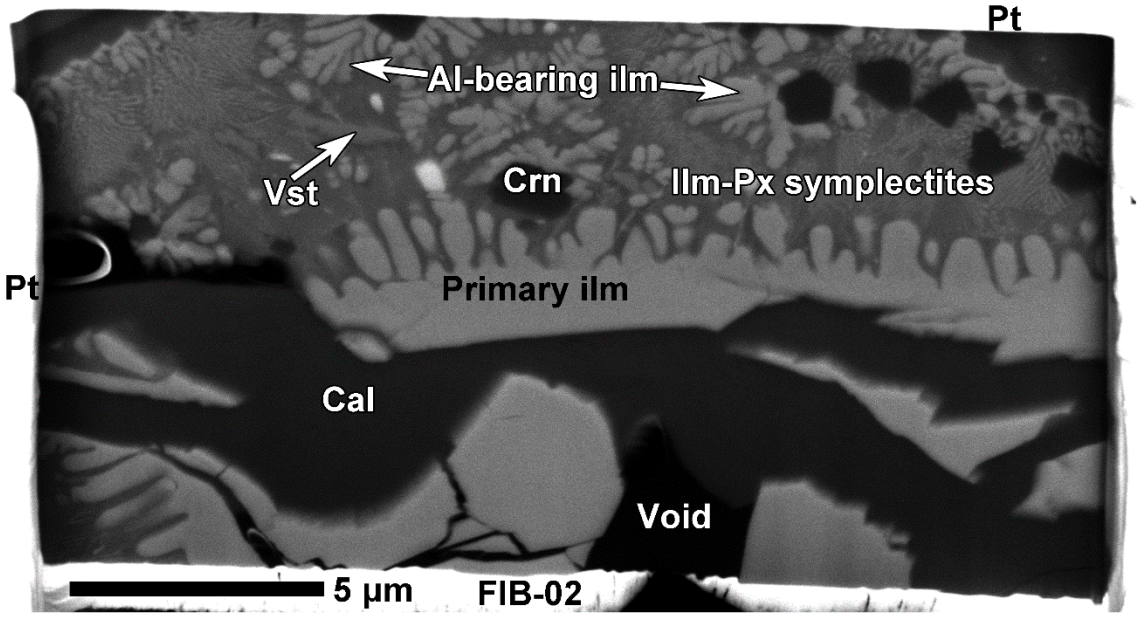

Figure 2

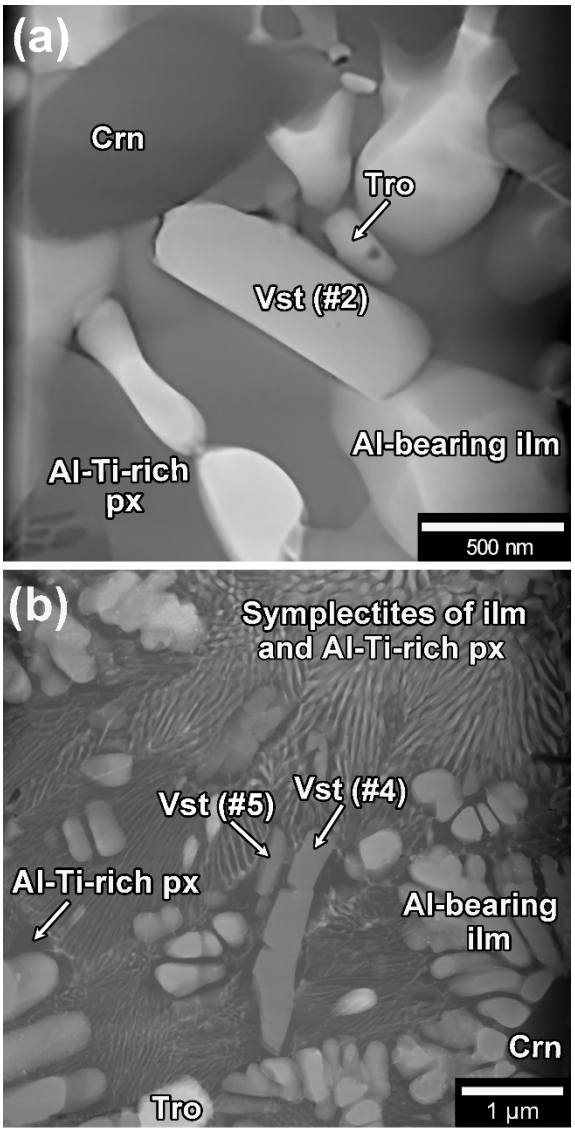

Figure 3

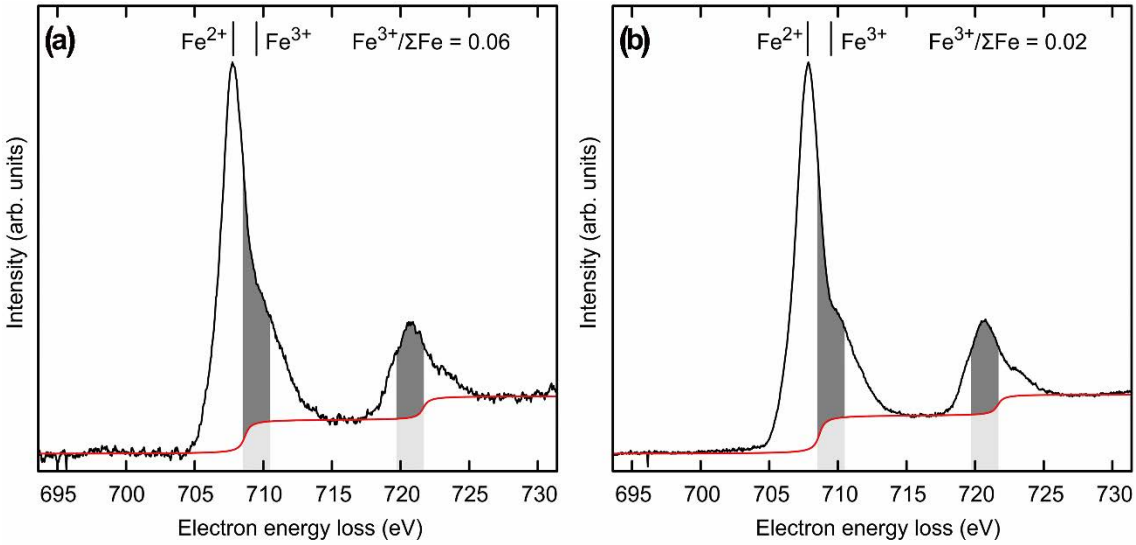

Figure 4

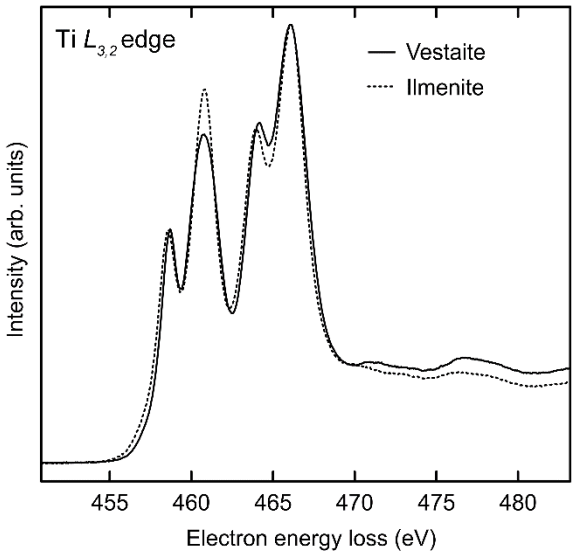

Figure 5

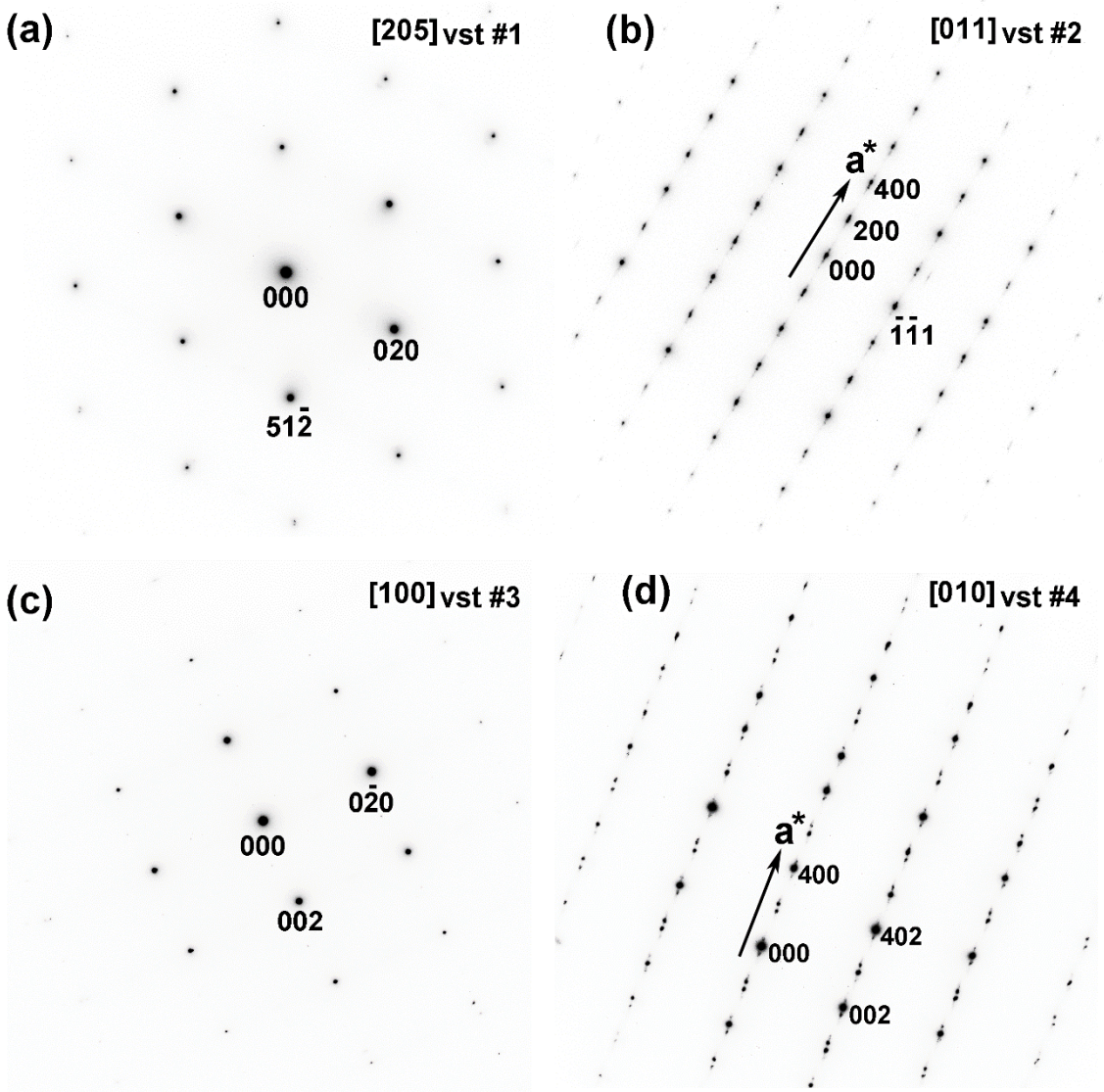

Figure 6

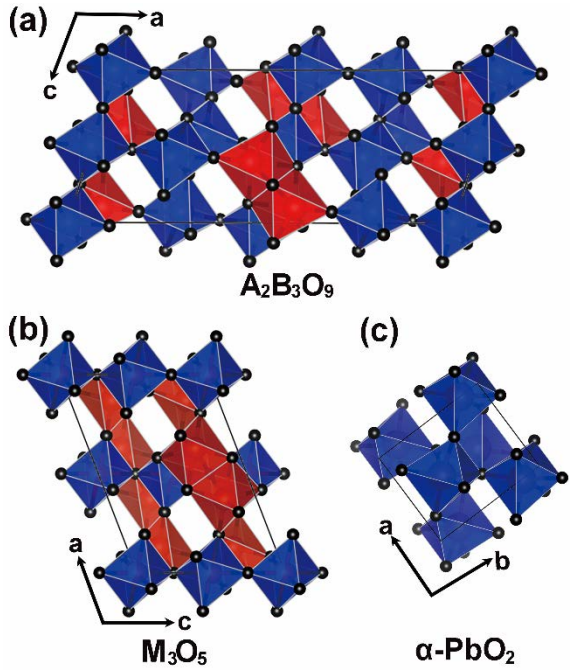

Figure 7

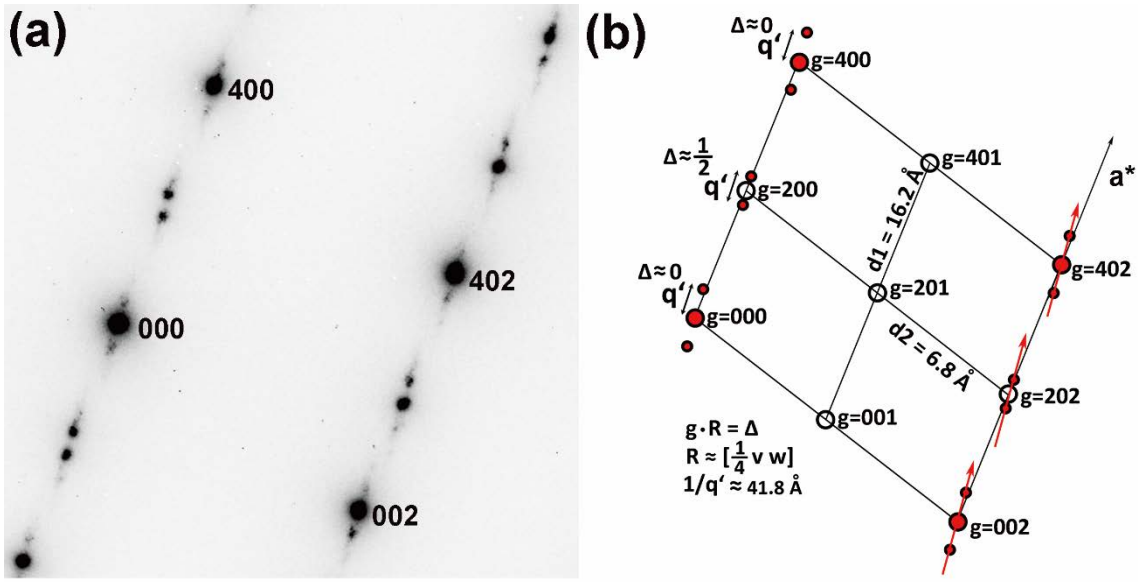

Figure 8

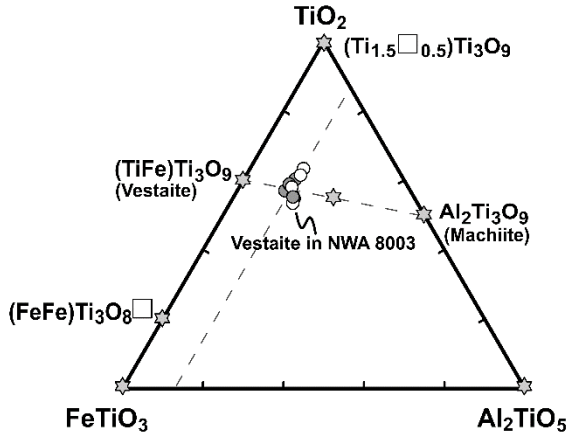

Figure 9

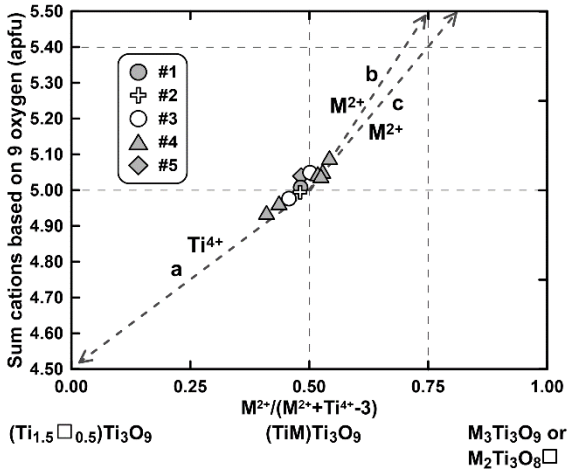

Figure 10

603

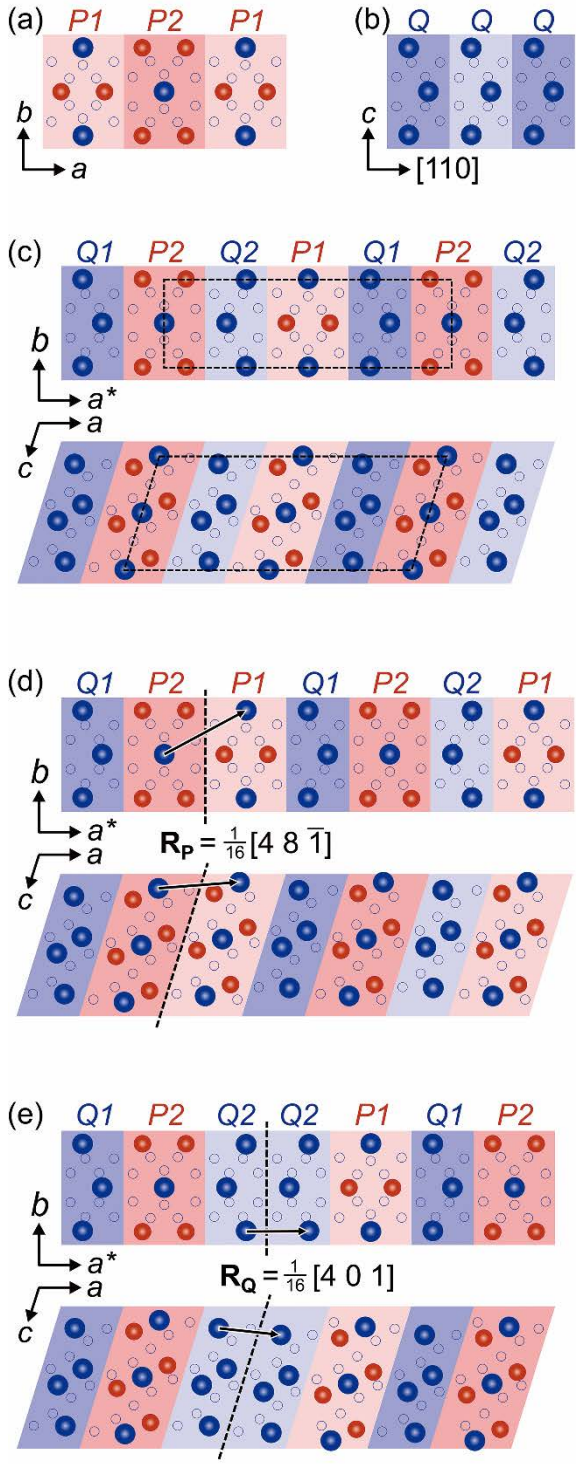

Figure 11

604